JOURNAL OF AIRCRAFT
Vol. 45, No. 1, January–February 2008

Aerodynamic Modeling of the Wing–Propeller Interaction for a Tail-Sitter Unmanned Air Vehicle

R. Hugh Stone*
University of Sydney, Sydney, New South Wales 2006, Australia

DOI: 10.2514/1.15705

This paper considers the aerodynamic modeling of a twin-engine tail-sitter unmanned air vehicle that relies on wing- and fin-mounted control surfaces submerged in the propeller slipstreams for control during low-speed vertical flight. The aerodynamic forces on this vehicle are predicted using a full azimuthal blade-element solution for the propellers combined with a fixed-wake panel-method model of the vehicle itself. When the flow components determined from the propeller solution are superimposed on the external flowfield and integrated with the panel-method model, the aerodynamic forces can be determined for the full vehicle, including slipstream effects, which are dominant in low-speed flight. The modeling described in this paper has been used extensively for multidisciplinary optimization work, as well as in the construction of a comprehensive aerodynamic database for the vehicle. This database encompasses all the aerodynamic force and moment coefficients and their derivatives for over 4300 separate flight conditions and has been extensively used for vehicle simulation and control design purposes.

Nomenclature

A = propeller-disc area or panel area
C_D = drag coefficient
C_L = lift coefficient
C_{L_0} = lift coefficient at $\alpha = 0$
D = drag force (parallel to the freestream)
L = lift force (normal to the freestream)
k_d = slipstream development factor
q = freestream dynamic pressure
R = propeller radius
r = propeller radial coordinate
S = planform area
s = distance aft of the propeller disc
T = propeller thrust
V = total freestream velocity
V_x, V_y, V_z = freestream x-, y-, and z-direction flow components
v_{ia} = induced axial velocity at disc
X, Y, Z = standard body axes directed forward, starboard, and down, respectively
x, y, z = aircraft axes directed aft, starboard, and up, respectively
α = angle of attack
α_{eff} = effective angle of attack
β = angle of sideslip
ΔV = velocity increment due to the propeller
ρ = density

Subscripts

i = inviscid value
v = viscous (corrected) value
row = value summed over a chordwise row of panels

Superscripts

$'$ = slipstream value

I. Introduction

THE T-wing is a tail-sitter unmanned air vehicle (UAV) concept that has been undergoing development at the University of Sydney since 1995 [1] (Fig. 1). It is designed to take off and land vertically, but spend the mission portion of its flight in a conventional horizontal flight attitude. Although the vehicle is somewhat similar to the Boeing Heliwing of the early 1990s [2,3], it is fundamentally different in its mode of hover control. Whereas the Heliwing vehicle used conventional cyclic rotor controls, the T-wing uses control surfaces submerged in the slipstream of its propellers in a fashion reminiscent of the early Convair XF-Y1 [4] and Lockheed XF-V1 [5] tail-sitters of the 1950s. For this reason, the prediction of the slipstream effects is critical to the successful modeling of the vehicle aerodynamics.

Numerous studies have been conducted into the problem of propeller–wing interaction, however, these have mostly been in the context of conventional aircraft in horizontal flight. In the 1970s, McVeigh et al. [6] presented a lifting-line method to predict the span-loading effects of propellers on wings up to stall. They used a blade-element solution coupled with a lifting-line approach. In the 1980s, Kroo [7] looked at the interaction of wings and propellers to determine optimum efficiencies for propeller rotational direction and optimal wing-twist distributions in the presence of a propeller slipstream. He also used a blade-element propeller solution coupled with a lifting-line-wing model. Witkowski et al. [8] solved the wing–propeller interaction by using a full vortex-lattice solution of both the wing and propeller simultaneously, averaged over many different propeller rotational positions. In this case, the propeller used a fixed helical wake. Because the propeller and wing solutions were solved simultaneously, this methodology captured not only the propeller effect on the wing, but also the wing effect on the propeller. Good agreement with experimental data was obtained up to stall, after which the purely inviscid vortex-lattice-method solution generated significant errors.

In the 1990s, Ardito Marretta [9–11] used a free-wake propeller solution in which both the propeller and wing were modeled using a Weissinger version of the normal Prandtl lifting-line model (effectively, a vortex-lattice method solution with only one chordwise panel). The propeller-wake model used by Ardito Maretta was based on the work of Favier et al. [12]. Although this relied on

---

Presented as Paper 5951 at the International Powered Lift Conference, Williamsburg, VA, 5–7 November 2002; received 7 May 2007; revision received 16 July 2007; accepted for publication 17 July 2007.

*Lecturer, School of Aerospace, Mechanical and Mechatronic Engineering, Building J07. Senior Member AIAA.

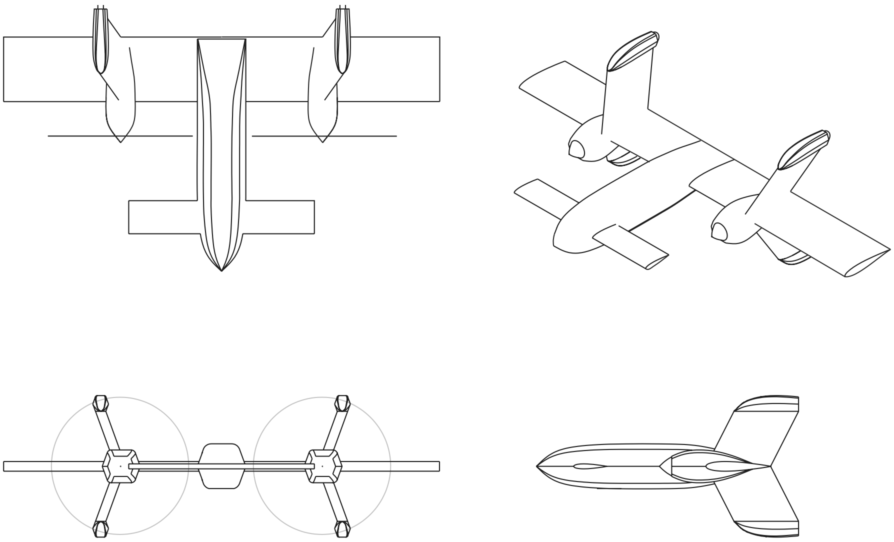

Fig. 1 T-wing vehicle configuration.

some empirical data to locate the tip-vortex position and the far-wake region of the flow, it still allowed for the propeller vortex sheet to be placed tangent to the flow in the near-wake region. In doing so, this free-wake solution ensured a force-free wake, in contrast to the prescribed propeller-wake assumptions of Witkowski et al. [8], while still allowing simultaneous solution of propeller and wing aerodynamics. The reliance on a prescribed tip-vortex location (based on empirical data) was obviated by Simonetti and Ardito Marretta [13] by using shape functions to describe the propeller wake. The error in flow tangency to the vortex sheet was then minimized by adjusting the shape-function coefficients using an iterative procedure. In all these cases, the emphasis was on conventional aircraft for which the solutions were able to determine a number of detailed features of the interaction. Some of these features are the relatively small perturbations caused to the steady-state wing and propeller solutions, the vibratory loads that result from the propeller and its wake passing in front of the wing, and the detailed geometry of the near wake of the propeller in the presence of the wing.

In terms of vertical takeoff and landing vehicles, a significant amount of work, both experimental and theoretical, was done in the 1950s and 1960s. Much of this work is summarized in McCormick [14]. Ardito Marretta et al. [15] used a free-wake analysis to study the interaction for a tilt-rotor type of vehicle for a range of flight conditions from forward flight to hover, though always at low angles of attack with reference to the wing. Recently, Hunsaker and Snyder [16] developed a similar methodology to the current work, which uses a lifting-line approach for the wing, coupled with a blade-element propeller solution. It allows for poststall aerodynamic effects to be captured by iteratively solving the lifting-line equations, using known 2-D lift data. This method (with the addition of the propeller flowfield) is similar to that outlined by Phillips and Snyder [17]. Although the work of Hunsaker and Snyder [16] is directed at finding solutions for tail-sitter-type vehicles, results are only presented for relatively low angles of attack.

The author [1,18] developed the current methodology during the late 1990s and early 2000s to analyze the T-wing concept-demonstrator UAV, which to date has achieved autonomous vertical and horizontal flight. Flight test pictures of this vehicle are given in Fig. 2.[†] This work uses a full azimuthal blade-element propeller solution coupled with a standard low-order panel-method model to directly solve the flows for wing-in-propeller-slipstream vehicles. The propeller blade-element solution is used to predict the propeller forces and moments in all axes, as well as the slipstream flow components (radial and tangential) that have to be added to the flow to simulate the slipstream effects on the wing and fin surfaces. This is shown diagrammatically in Fig. 3. Through the use of careful spatial matching between the contracted slipstream and the panel model grid, it is possible to obtain smoothly varying aerodynamic coefficients and derivatives (except those for $\dot{\alpha}$ and $\dot{\beta}$) over a large

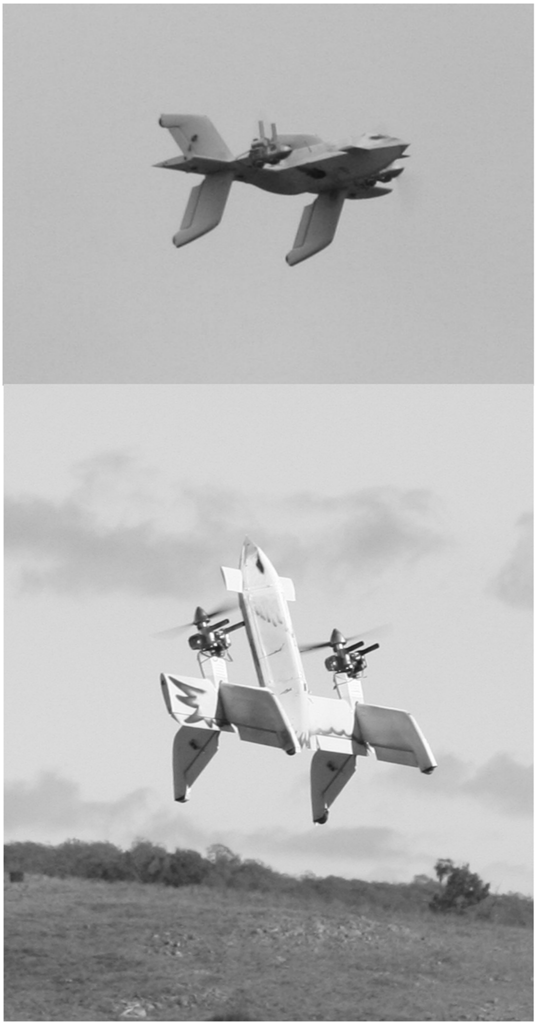

Fig. 2 T-wing concept-demonstrator vehicle in horizontal flight at $\sim 120\ \mathrm{ft/s}$ (top) and in vertical descent at ($\sim 4\ \mathrm{ft/s}$) just before landing (tilting into wind).

[†] Videos of various T-wing flight tests are available online at www.aeromech.usyd.edu.au/uav/twing [retrieved 10 Sept. 2007].

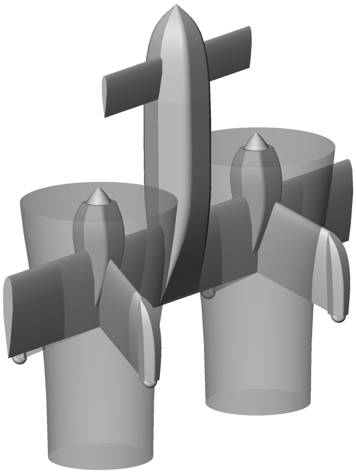

Fig. 3 Slipstream interactions with wings and fins.

range of flight conditions from vertical descent to high-speed horizontal flight.

Although the approach adopted here shows similarity with many of the preceding methodologies, the use of 2-D experimental airfoil data to correct the inviscid panel-method solution in those regions well outside the bounds of normal linear aerodynamics has allowed it to be used through a much greater range of flow conditions than in previous work. This is particularly important in low-speed vertical flight, in which translational vehicle velocities or wind components give rise to angles of attack or sideslip on the order of 90 deg in the nonslipstream regions. To address such issues in a consistent way that allows a seamless analytical method to be applied across the full T-wing flight envelope, 2-D viscous corrections are applied to the linear panel-method results, even at extreme angles of attack. Although there are known deficiencies with this approach, tests have shown that the method is sufficiently accurate to produce reasonable predictions for the (usually) second-order effects of the loads in the nonslipstream regions. Comparison with experimental data suggests that results are accurate enough for preliminary design trade studies, simulation, and control development work.

One of the chief advantages of the approach outlined vs more sophisticated flow-solution techniques is that it is computationally economic. This has made it suitable for use in multidisciplinary optimization (MDO) work [19] and in the construction of large aerodynamic databases for flight simulation of the T-wing UAV. Such a database, ranging over 4300 separate flight conditions of varying speeds, flow angles, and throttle settings, can be constructed in a single computer run, taking ~2 h with a standard 2.0-GHz PC.

Finally, it should also be stated that because there are no suitable wind-tunnel facilities available to conduct hover and low-speed vertical flight-testing of a tail-sitter UAV at the University of Sydney, the results from the present analysis are the sole source of aerodynamic modeling for the development of the T-wing vehicle. As shown in Fig. 2, the actual test-demonstrator vehicle was successfully flown in vertical, horizontal, and transition flight regimes in full autonomous mode, with all controllers based on the results from the present aerodynamic analysis.

Section II of this paper outlines the propeller solution used in the present analysis, and Sec. III details how this is used in conjunction with the panel-method solution. The method is benchmarked against previously published experimental data in Sec. IV. Section V then presents detailed point results and aggregate results as used in simulation databases, with Conclusions given in Sec. VI.

II. Propulsion and Slipstream Model

The starting point for the method used in the present analysis is the blade-element solution for the propellers, and for this, an adaptation of Goldstein's vortex theory is used [20], with lookup tables for blade lift and drag coefficients based on the 75% blade-station Reynolds number. It has been found that more accurate results are obtained at low advance ratios if the poststall lift coefficient data are cut off at the stall value. This is consistent with the findings of others [20]. Standard compressibility corrections of the form $1/\sqrt{1-M_{\text{local}}^2}$ are applied to the blade lift and drag coefficients in the code. Because one of the main uses for the analysis described in this paper is the establishment of an aerodynamic database for an actual concept-demonstrator tail-sitter UAV, the propeller solution was iterated to enforce a match between the power absorbed by the propeller and the known power available curve of the engines in use.

Because a tail-sitter vehicle is required to operate over a large range of flow angles, a full azimuthal solution is used to capture the blade-element lift and drag variations around the disc due to nonaxial inflow velocities. Blade forces are then integrated both azimuthally and radially to give all six load components. The effects of body-axis rates on the propeller solutions (required for the prediction of rate derivatives) are also incorporated by superimposing virtual flow velocities on the external flow condition. For instance, for a yaw-rate condition, the starboard propeller will experience a negative average axial flow component added to the external flowfield, with a linear variation in the virtual velocities added from one side of the disc to the other. A similar virtual velocity field applies to the port propeller, but this time with a positive average axial component. In-plane virtual velocity components will also be generated, due to the offset in the fuselage station between the propeller discs and the c.g.

A. Slipstream Development

The amount of slipstream development was calculated using a simple formula suggested by McCormick [14]:

$$k_d = 1 + \frac{s}{\sqrt{s^2 + R^2}} \tag{1}$$

where k_d is the slipstream development factor, which tends to 2.0 as $s \to \infty$. The distance s was taken as the distance between the propeller disc and the wing midchord. Once the development factor is determined, it is possible to calculate the actual slipstream velocity distribution by applying conservation of mass and angular momentum to the annular stream-tube segments associated with each radial blade element. This procedure is exactly the same as that used by McVeigh et al. [6] except that the slipstream is not prescribed to be fully developed ($k_d = 2.0$). In this method, the inner edge of the stream tube corresponding to the inner station of the first blade element is initially set at the nacelle radius. The outer edge of the annular stream-tube segment corresponding to the first element is then determined to ensure conservation of mass within this annulus, given that the axial velocity is increased in relation to its propeller-disc value by the development factor. The radial location of the outer part of the annulus corresponding to the first element then becomes the inner radius for the annulus for the second element and the process is repeated until the entire contracted wake geometry *of the slipstream* has been determined. The geometry of the slipstream model is shown in Fig. 4. The slipstream stream-tube radial extent is calculated as described earlier and as set out in Eq. (2):

$$r'_m = \begin{cases} r_{\text{nacelle}} & m = 1 \\ \sqrt{r'^2_{m-1} + (r_m^2 - r_{m-1}^2)K_v} & m = 2, \ldots, n \end{cases} \tag{2}$$

where

$$K_v = \frac{[2V_x + v_{ia_m} + v_{ia_{m-1}}]}{[2V_x + k_d(v_{ia_m} + v_{ia_{m-1}})]}$$

The tangential velocity components in the slipstream are determined by noting that their velocities jump immediately behind the disc to twice their at-disc values and then are increased in proportion to the radial decrease in slipstream extent to preserve angular momentum. The axial velocities are simply increased in direct proportion to the development factor. The slipstream velocity profiles are given in Eq. (3):

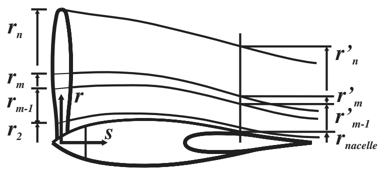

Fig. 4 Slipstream development quantities.

$$v'_{ia_m} = k_d v_{ia_m} \qquad v'_{it_m} = 2v_{it_m}\left(\frac{r_m}{r'_m}\right) \tag{3}$$

The following limitations relating to this methodology should be noted. First, in modeling the slipstream effect on the aircraft, no account is taken of mixing between the slipstream and external flows at the slipstream edge: this is beyond the scope of the present work. Second, the method presented relies entirely on the use of time-averaged slipstream velocity profiles: the real slipstream would consist of a time-varying helical wake made up of vortices that are continually shed by the propeller blades. The use of time-averaged velocity profiles is justified by considering that the dominant frequencies of the unsteady aerodynamic solution are related to the blade rotational frequency of approximately 100 Hz and thus well-separated from the vehicle rigid-body dynamic modes by several orders of magnitude. Finally, although the load solution is azimuthal, the propeller slipstream velocity profile is averaged around the propeller disk.

From the forgoing discussion it is clear that the propeller flowfield and load calculation procedure is much simpler than the prescribed wake analyses of Witkowski [8] or the free-wake analyses of Ardito Marretta et al. [9–11,13,15]. This makes it incapable of predicting either the detailed structure of the wake or the fine details of its interaction with the wing (such as vibratory loads and their phase relation to propeller azimuth). Further more, because the propeller solution is done in isolation from the wing, the effects of wing upwash on the propeller are ignored in terms of their effects on the propeller solution. Nevertheless, the current methodology is felt to represent an apposite solution for the calculation of first-order interaction effects for the purposes of rigid-body simulation and MDO analyses. In these cases, which require propeller solutions to be performed for many tens of thousands of flight conditions,[‡] calculational precision has been sacrificed for computational speed. The need to iteratively solve for a force-free wake in the more detailed free-wake methods mentioned for any given blade angle, as well as the need to perform such iterations over a range of blade azimuth angles to obtain time-averaged loads, makes these methods unsuitable for the present purpose.

Some typical propeller results for a cruise velocity of 120 ft/s and a (large) sideslip angle of 12 deg are shown in Figs. 5 and 6. The first of these presents the difference in thrust ($\mathrm{d}T/\mathrm{d}r$) between the azimuthal and nonazimuthal solutions around the propeller disc, and the second shows the variation of in-plane load in lbf/ft. (At each element in the disc, the in-plane load is directed tangentially opposite to the direction of rotation.) By integrating these two load components around both discs, all six load components for each propeller are obtained. These loads are then transferred to an appropriate aircraft axis system (e.g., the c.g. body-axis system) to be added with the loads from the panel-method solution. Looking at the *starboard* propeller in Figs. 5 and 6, it can be seen that the thrust and in-plane loads are biased to the top of the disc, on which the local blade angle of attack is greatest, due to the sideslip. For this propeller *in isolation*, this would thus result in an overall negative F_y force and a negative (pitching down) M_y moment, along with the usual thrust F_x and torque M_x loads.

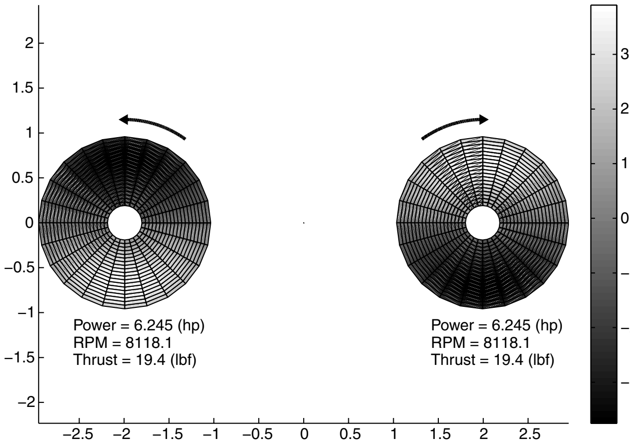

Fig. 5 Variation of thrust around the disc; difference between the azimuthal and nonazimuthal solutions; forward flight and 10-deg sideslip; view looking forward.

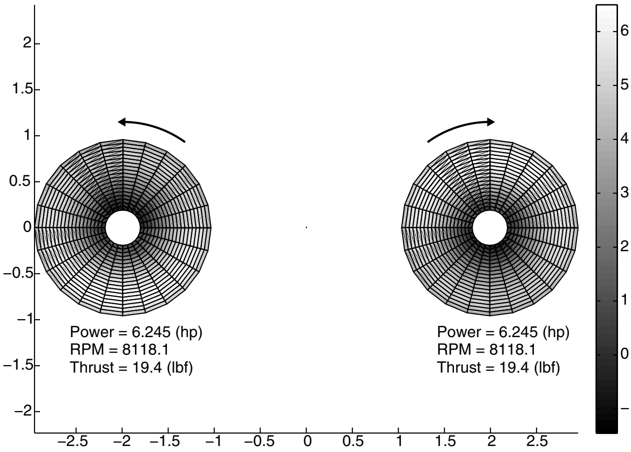

Fig. 6 Variation of disc in-plane loads; forward flight and 12-deg sideslip; view looking forward.

B. Propeller and Wing Interaction

One of the most important features of the present analysis is the interaction between the propeller slipstream and the wing in low-speed flight. Because a wing-in-slipstream vehicle depends on the prop wash over wing- and fin-mounted control surfaces for its hover controllability, the accurate prediction of this interaction is critical to the successful design and simulation of the vehicle. To simplify the analysis, a number of reasonable assumptions are made. These are detailed next.

1) The nacelle's axes are assumed coincident with the wing chord line, thus meaning that axial and tangential flow velocities are parallel and normal to the wing chord, respectively.

2) The propeller slipstream is assumed to affect the main wing only and not the canard (for which any propeller-induced velocities are significantly lower).

3) Only the propeller effects on the wing are modeled: the wing upwash and canard downwash effects on the propeller are ignored. For a symmetric flight condition, these induced flow velocities would produce yawing moments, which are balanced for two contrarotating propellers. Furthermore, for vertical flight conditions, in which the slipstream effects are most critical, the canard downwash will be negligible due to the low flow velocities over it, whereas the wing-upwash terms will be small due to the separation of the wing and propeller disc. There would be a significant increase in computational burden were the wing- and canard-induced velocities included in the solution, because these would require iteration

---

[‡] For instance, a typical MDO analysis may require 2000 full vehicle calculations (including line searches and finite differencing over the design variables), each requiring two propellers to be solved for three fundamental flight conditions, each with eight attendant perturbation cases to capture aerodynamic derivatives. This gives a total of $2000 \times 2 \times 3 \times (1 + 8) = 108,000$ individual propeller solutions, though some reduction of this number may be possible.

between the propeller blade-element and panel-method solutions. In the current computational scheme, the blade-element solution is determined first and its flow velocities are simply added to the external flow used in the panel-method code.

4) The slipstream development (contraction) is fixed at the value given previously from Eq. (2); no chordwise variation of the slipstream is assumed.

5) The propeller-induced velocities, both axial and tangential, are added to the freestream velocity components to give the flowfield for the wing elements of the panel-method model. For that region of the *wing* immersed in the slipstream, the axial-induced velocities increase the local chordwise velocity and the tangential velocities (representing swirl) alter the local angles of attack. It should be noted that both these velocities vary with radial position in the slipstream. It should further be noted that although a full azimuthal blade-element solution was performed, the axial and tangential velocity profiles of the slipstream were averaged around the disc to give axisymmetric velocity distributions for the purposes of slipstream interactions with the panel-method model. This is expressed by Eqs. (4), which give the Cartesian flow velocities at a particular panel control point as a function of the freestream velocity components V_x, V_y, and V_z, the radially varying propeller slipstream axial and tangential velocities v'_{ia} and v'_{it}, and the cylindrical coordinates r and θ of the point in the slipstream.

$$\begin{gathered} v_x = V_x + v'_{ia}(r) \qquad v_y = V_y \mp v'_{it}(r)\sin\theta \\ v_z = V_z \pm v'_{it}(r)\cos\theta \end{gathered} \tag{4}$$

Equation (4) assumes an aerodynamic axis system (x aft, y starboard, and z upward) and takes θ as increasing from the positive y axis to the positive z axis. The dominant signs for the tangential velocity component terms correspond to a propeller rotating clockwise when viewed from the front.

It is assumed that the slipstream axis remains coincident with the propeller axis or, in other words, that the slipstream does not get blown away from the wing. This assumption is reasonable provided that the freestream normal velocity is not too great in relation to the total slipstream axial velocity and that the propeller disc is not too far in front of the wing. This is expressed by the following inequality:

$$V_z \ll \left(\frac{R}{s}\right)(V_x + v'_{ia}) \tag{5}$$

Provided that this condition is satisfied, it is felt that the method will provide reasonable results.

A diagram of the addition of the propeller-induced *slipstream* velocities to the freestream flow components that produce the full input flow for the panel-method model is shown in Fig. 7 for a winglike surface behind the propeller. In this case, the freestream flow is shown with an angle of attack but no sideslip. The extension of this procedure to other surfaces such as fins is straightforward and covered by Eq. (4). (For right-angled fins, the slipstream tangential components will add to and subtract from the y component of freestream flow due to sideslip.)

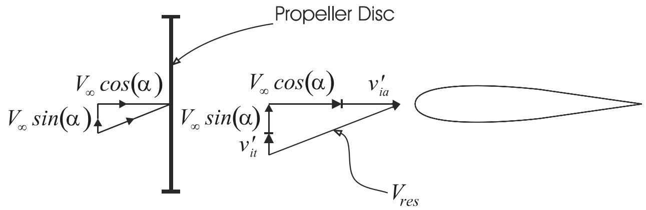

Velocity Diagram: Upgoing Blade Side of Propeller

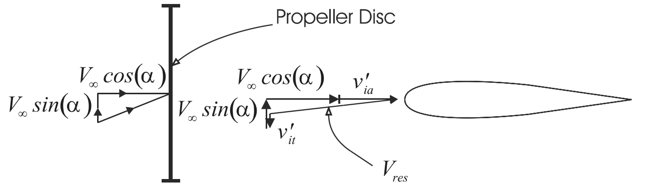

Velocity Diagram: Downgoing Blade Side of Propeller

Fig. 7 Addition of propeller-induced slipstream velocities to freestream flow for the wing surface behind the propeller.

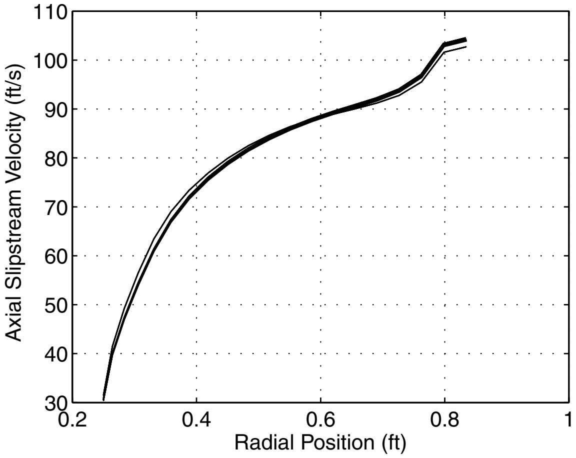

Fig. 8 Propeller slipstream axial-induced velocity distribution.

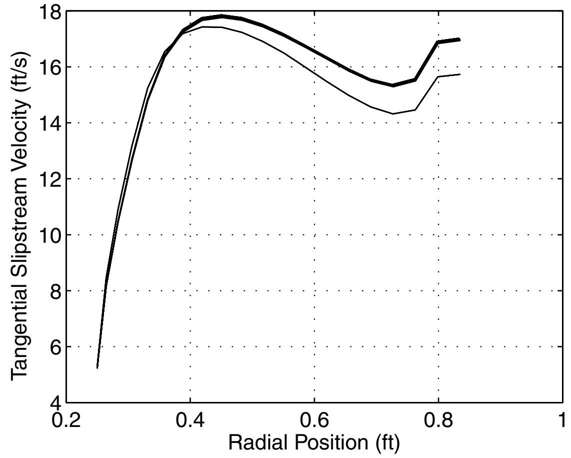

Fig. 9 Propeller slipstream-induced tangential velocity distribution.

Plots of typical slipstream-induced velocity distributions are given in Figs. 8 and 9. These are for the concept-demonstrator T-wing vehicle hovering in a vertical attitude with a 20-ft/s flow normal to its wing ($\alpha = 90$ deg) at a throttle setting of 0.57 (the power is 1935 ft × lb/s, the rpm is 5325, and the propeller diameter is 25 in.). Aerodynamic results for this particular flow condition, which approximates that of the vehicle hovering in a moderate crosswind, are given later. A variety of different curves are shown on the plots and represent the slightly different velocity fields produced for perturbations about the basic flow condition. The different velocity fields are used to determine aerodynamic derivatives with respect to the flow parameters, body-axis rates, and propeller control variables (namely, throttle and blade pitch[§]). To allow for easier integration with the panel-method model described later, the edges of the perturbation slipstream distributions are adjusted to match those of the basic case by enforcing a continuity condition on the adjustment. Finally, Fig. 10 shows the wake from a single propeller blade that corresponds to these velocity profiles for the hover flight condition of Figs. 8 and 9 and the slipstream contraction Eq. (2). Although this figure shows a helical contracting wake, it must be clearly understood that the actual wake velocity values were fixed at those obtained at

---

[§] On the current concept demonstrator, blade-pitch derivatives are not used because the propellers have fixed pitch.

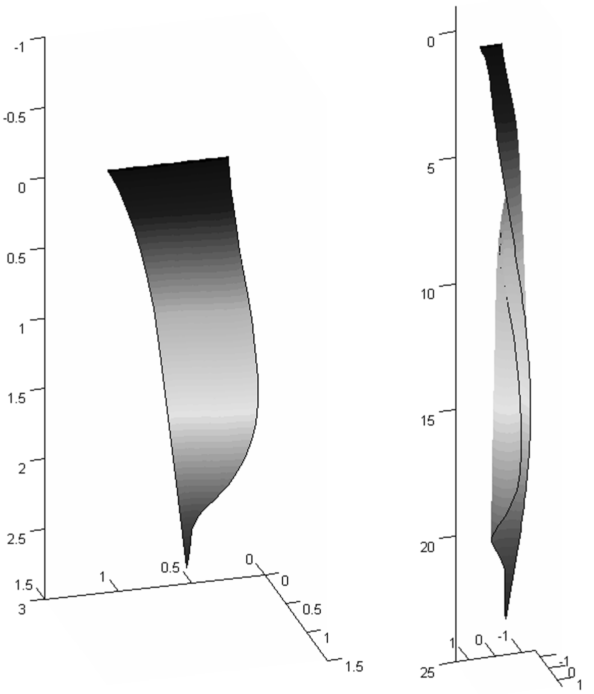

Fig. 10 Wake development from a single blade in hover: near region and extended wake; blade at the top with the tip on the left in both cases (dimensions in feet).

one y–z plane (coincident with the wing midchord) behind the propeller. The picture has been included for completeness and shows a close-up of the wake in a region that includes the wing, which lies between 1.05 and 2.15 ft behind the propeller face, as well as a much more extensive view in which the helical structure is more evident. These wakes are generated purely from blade-element velocity profiles and do not account for the known collapse of the wake into a turbulent far-wake region as detailed in other studies [12].

III. Aerodynamic Model

The aerodynamic modeling of the T-wing vehicle uses a low-order fixed-wake panel model. This is used to determine aerodynamic forces and derivatives for an arbitrary flight condition. The current method uses thin lifting surfaces modeled using vortex-ring elements, together with a horseshoe-vortex wake [21]. The wake is constrained either to lie in the vehicle horizontal reference (x–y) plane or to leave the trailing edge parallel to the freestream velocity. To avoid complex modeling considerations, the vehicle body is modeled as a simple cruciform arrangement of width and height equal to half the body diameter for a nominal vehicle with a round fuselage. For the current concept-demonstrator vehicle, which has a diamond-shaped fuselage with sharp sides but rounded top, the modeled fuselage width is made the same as the body. This model is shown in Fig. 11. As discussed later, even significantly coarser grids than this give acceptable results.

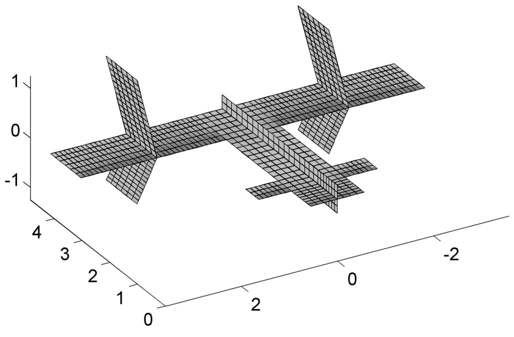

Fig. 11 Concept-demonstrator T-wing model with a cruciform body (dimensions in feet).

In other work using simple low-order panel-method models for MDO work, Gallman et al. [22,23] use models with only one chordwise panel. For MDO work using gradient-based optimization, this allows accurate derivative information to be obtained with respect to wing sweep and taper. In contrast, for models with multiple chordwise elements, as the taper and sweep change, the projection of the bound vortex segments for one wing may shift to the other side of the control points of elements in the opposite wing. This produces spurious local peaks and troughs in the aerodynamic loads. This destroys the possibility of obtaining accurate gradients via finite differences and will occur even if the actual singularity condition is handled using some form of vortex-core model.

For the modeling of the T-wing, several chordwise elements are used. This is done because during low-speed vertical flight the dominant aerodynamic loads are confined to the low-aspect-ratio regions submerged in the propeller slipstreams. Similar to the modeling of low-aspect-ratio wings, it is felt that the use of multiple chordwise panels would model these regions more accurately than the use of a single chordwise panel. The use of multiple chordwise panels is also necessitated by the need for extra zones for control surfaces, to allow their derivatives to be determined. (To obtain control surface derivatives without multiple chordwise panels, a lifting-line solution can be used, as suggested by Phillips [14].)

In the current model, the fins present the only problem with respect to the use of multiple chordwise elements, because these are the only swept surface on the vehicle. Because of this, the fins are artificially unswept in the panel model and then the various load coefficients and derivatives are corrected based on a rational assessment of the effect of fin sweep on both their centers of pressure and on their local lift-curve slope.

Computational efficiency has always been a key goal of the modeling effort for the T-wing UAV. To this end, it is necessary to be able to calculate all aerodynamic derivatives (with the exception of $\dot{\alpha}$ and $\dot{\beta}$) in a single aerodynamic solution that involves building and solving the aerodynamic influence coefficient matrices only once. This is accomplished by using auxiliary load cases, which contain flow perturbations added to the fundamental flowfield that correspond to each of the derivative conditions. The derivatives are then obtained by finite differencing the results from the auxiliary cases with the fundamental case. The first six auxiliary load cases are constructed easily by uniformly perturbing the external flowfield in the case of the V, α, and β derivatives and by adding virtual velocities to the basic flow for the cases corresponding to the angular rate derivatives P, Q, and R. The auxiliary cases associated with deflected control surfaces are constructed without changing the basic model geometry (i.e., without deflecting the control surface panels) by deflecting the flow vector at each control surface panel to give it the same flow angle relative to the control surface as if the panel itself had been deflected about its hinge line. Finally, the auxiliary load cases associated with throttle or propeller collective pitch derivatives are simply formed by using the flowfields obtained from the propeller model for these derivative conditions instead of the basic condition.

For the flow and rate derivative cases, different propeller flowfields corresponding to the different derivative conditions are used. Thus, for instance, in calculating yaw-rate derivatives, propeller flowfields corresponding to the yawing condition must be used on each wing. Thus, for a positive body-axis yaw-rate condition (vehicle yawing to the right), an overall perturbation flowfield is added to the basic flow to represent the relative motion of the vehicle in the air, with different propeller flowfields for each wing. The retreating (starboard) wing will see a slight negative average virtual velocity field but slightly higher propeller-induced velocities in comparison with the port wing. This is because the retreating propeller will generate higher induced velocities than those of the advancing propeller.

For the model to be useful for calculating aerodynamic derivatives due to small flow perturbations or for calculating geometric design sensitivities for MDO work, considerable care must be taken in developing the aerodynamic grid. This is due to the nature of panel-method solutions, which involve the superposition of elemental flowfields, many of which involve singularities. Even if the actual singularities of vortex elements, for example, are removed via the use of a vortex-core model, this still does not prevent the panel model from being overly (and incorrectly) sensitive to slight physical or flow geometry changes. This is essentially because the boundary conditions sample the flow solution (in determining influence coefficients) at a spatial frequency that is always less than the spatial frequencies present in the elemental flowfields.

To circumvent this problem, it is necessary to align the grids between different surfaces so that the element control points and the trailing vortices from different surfaces always have the same fixed relation to each other. To allow design sensitivities to be determined for MDO work as the basic geometry of the vehicle changes, the lifting surfaces are divided into zones, within which the spanwise distribution of panels remains constant, that are aligned between different regions separated in the streamwise direction. Thus, when the canard span is altered slightly for a sensitivity calculation, not only are its panels stretched slightly, but so are those in the corresponding zone on the wing surface behind it. This technique makes it possible to produce smooth, correct sensitivity information for MDO work.

For the T-wing model, further zone boundaries are required on either side of the propeller slipstream velocity distribution, because the velocity distribution has a sharp edge, which causes spurious sensitivities to its size and positioning. This can be appreciated by considering the case of a slipstream velocity distribution corresponding to a constant-throttle propeller solution being applied to a wing with a fixed grid. As the external flow velocity is increased, the amount of slipstream contraction will decrease and hence the slipstream at the wing will steadily grow. At certain velocities, the slipstream edge may cross the control points of particular rows of wing panels, thus causing sudden jumps in the velocities experienced by these panels. This will cause nonsmooth outputs in the panel-method solution. However, if the slipstream edges are always tied to the edges of particular panel zones, and if the number of panels in each zone is held constant, then good sensitivity information can be obtained. This is also indicated in Fig. 12.

For MDO solutions, the number of panels per zone must be held constant during finite difference calculation, as well as possibly during line-search routines. After each major optimization step, repaneling can be performed to ensure that reasonable panel aspect ratios are maintained. The problems are less severe when building simulation databases, because the actual vehicle geometry is fixed and the only zone boundaries that change are those associated with the slipstream.

The last main area of the methodology used that needs to be discussed is the application of 2-D corrections to the inviscid panel-method results. It needs to be understood clearly at the outset of this discussion that the corrections discussed are not meant to be highly accurate: *rather, they are meant to be first-order engineering corrections for the regions of gross error in the inviscid panel-method solution*. Usually, the regions of greatest error are those outside the slipstream in low-speed vertical flight. For instance, for a vehicle hovering in a steady crosswind, both the canard and the wing regions *outside the slipstream* will experience angles of attack in the vicinity of 90 deg. Because such regions are typically of much less significance than the slipstream regions in terms of the loads generated, the roughness of the corrections applied is less important.

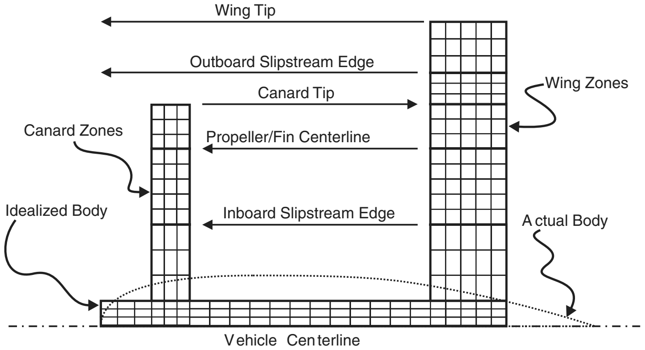

Arrows indicate projection of zone information from one surface to the next. Paneling is constant for the wing and canard in the same span-wise zones.

Fig. 12 Spanwise paneling for the aerodynamic grid.

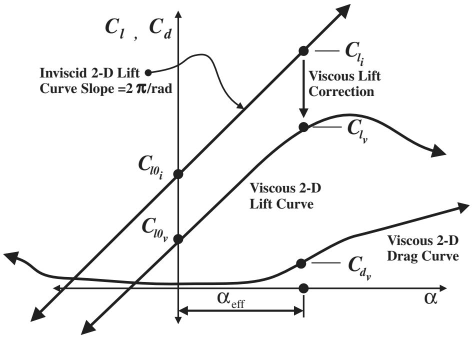

Fig. 13 Two-dimensional viscous correction procedure for panel-method solution results.

The method of correction is shown diagrammatically in Fig. 13. The correction is based on known viscous 2-D lift data obtained from the experiment, along with known inviscid 2-D panel-method data for the strip of panels in question, accounting for any control surface deflections. Once the normal inviscid panel-method solution has been performed, the local inviscid lift coefficient for each chordwise strip of panels is calculated. This allows the local angle of attack for this chordwise row to be calculated based on its known inviscid 2-D zero-lift angle and the 2π lift-curve slope. Table lookup then gives the corresponding viscous lift and drag coefficients for this local effective angle of attack, and the additional viscous loads are then distributed among the chordwise strip of panels in a rational manner. [One way to decide on the distribution of the extra viscous load is to match the final viscous pitching moment of the strip of panels with known viscous pitching-moment data. Another simpler (but less accurate) method is to distribute loads to match the distribution of the inviscid solution.] This procedure is summarized in Eq. (6):

$$\begin{aligned} C_{l_i} &= \frac{L_{\mathrm{row}}}{q_{\mathrm{local}} A_{\mathrm{row}}} \qquad & \alpha_{\mathrm{eff}} &= (C_{l_i} - C_{l_{0i}})/2\pi \\ C_{l_v} &= C_{l_v}(\alpha_{\mathrm{eff}}) \qquad & C_{d_v} &= C_{d_v}(\alpha_{\mathrm{eff}}) \end{aligned} \tag{6}$$

The lift and drag data used for the 2-D corrections are based on experiments for NACA 0012 sections over a range of flow angles from 0 to 180 deg [24]. The base lift and drag data are modified to account for changes in C_{l_0}, $C_{l_{\max}}$, and C_{d_0}, with control surface deflection as outlined in a variety of sources [25,26].

Although the primary importance of the corrections determined by this methodology is in the regions outside the slipstream during low-speed vertical flight, the method also ensures that control surface effects are not overpredicted by relating these back to known 2-D experimental data.

There are a variety of known shortcomings to the approach described. First, because the method makes no attempt to iterate between the inviscid solution and the viscous corrections, the circulation calculated for the purely inviscid solution is never adjusted based on the corrections. This means that the circulation associated with panels in stalled flow regions may be significantly in error because it is calculated from the inviscid solution only. This incorrect circulation will then induce erroneous velocities at all the other panels in the flow.

To circumvent this, some form of iteration would have to be performed between the inviscid solution and the 2-D corrections. This has been done for lifting-surface solutions employing only one chordwise panel in which a lifting-line boundary condition is applied instead of a zero normal-wash boundary condition [17]. An iterative approach has not been attempted here because solution speed has always been a prominent consideration in the development of the methodology.

The most serious potential result of these problems lies in the erroneous downwash that the canard wake will induce on the wing panels. To overcome this problem, the wake of all panels outside the slipstream region is constrained to follow the freestream direction instead of the local chordwise direction. This is physically more sensible, especially at large flow angles, and means that the extraneous downwash velocities in the wake have a smaller effect on the overall vehicle solution. Within the slipstream region, the wake vortices are set parallel to the chord plane to avoid having a raft of individual vortex segments, all at differing angles based on the slipstream angle-of-attack distribution. Because the angles of attack in this region are usually within the bounds of standard linear aerodynamics, this is judged to be a reasonable approach.

Another shortcoming of the proposed approach is that wing stall is known to involve significant 3-D effects [21]. Thus, the use of purely 2-D stall predictions cannot hope to model actual stall behavior properly. Considering these shortcomings, the real question then becomes one of whether the method is suitable for preliminary design and control development purposes. This can be judged by examining the lift and drag predictions produced by the method over a range of angle-of-attack conditions.

IV. Comparison with Experimental Data

To assess the accuracy of the methodology, it was compared against experimental results obtained from [27]. This particular report details tests of the flap effectiveness for a tapered wing with two overlapping propellers along the semispan and with 30%- and 60%-chord flaps. It presents lift, drag, and pitching-moment results for different propeller thrust settings, different freestream velocities, and for angles of attack between −10 and 90 deg. Because the present methodology has not been adapted to cope with overlapping propellers, only results for the single inboard propeller operating in conjunction with the 30%-chord flaps were considered in the comparison. It should be noted that these results are particularly pertinent for the T-wing test-demonstrator vehicle because the chord is similar, the size of flaps are the same, the airfoil (NACA 0015) is the same, and the propeller thrust is similar as well. Thus, besides being a generic test for the methodology, the results also closely match the actual magnitude of forces for the current T-wing vehicle. A picture of the panel model (without propellers) for this case is given in Fig. 14. The two darker-colored zones on the wing are the slipstream zones, which use vortex-ring panels with trailing vortices parallel to the chord; the remainder of the wing uses vortex-ring panels with trailing vortices parallel to the freestream velocity. In this figure, the vortices outside the slipstream region were given a nominal angle of 15 deg to the chord plane. This angle varies for each different freestream flow angle.

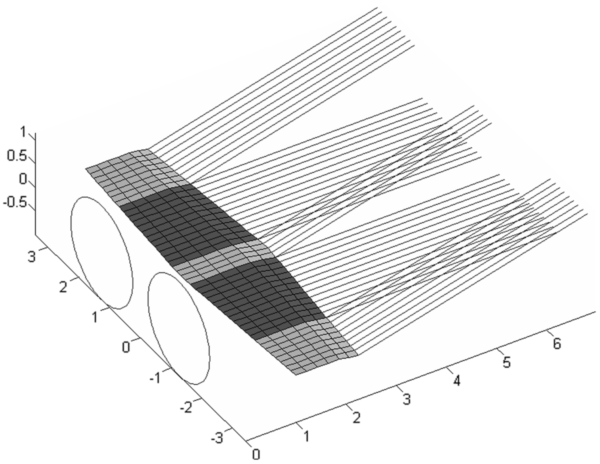

Fig. 14 Panel model for [27] comparison with inboard propellers (dimensions in feet).

Table 1 Test conditions for comparison with [27] measured results

T''_C	V, ft/s	$V+\Delta V$, ft/s	q'', psf	$\Delta V/V$	T, lb
0.71	44.2	82	8	0.855	17.6
0.91	24.6	82	8	2.333	22.6

The results presented use nondimensional coefficients, in keeping with the original presentation of the data in [27] (in which the longitudinal force in the opposite direction to drag is used). To avoid singularities because the freestream dynamic pressure tends to zero, force coefficients based upon the slipstream dynamic pressure q' were used, as shown next:

$$q' = q + \frac{T}{A_D} \qquad T'_C = \frac{T}{q' A_D} \qquad C'_D = \frac{D}{q'S} \qquad C'_L = \frac{L}{q'S} \tag{7}$$

where q' is the slipstream dynamic pressure, T'_C is the thrust coefficient, C'_D is the drag coefficient, and C'_L is the lift coefficient.

Results are presented for flap settings of 0 and 10 deg and for thrust coefficients of 0.71 and 0.91. According to [27], the calculated data were constructed by varying the propeller rpm to keep thrust constant throughout the full angle-of-attack range, with the slipstream dynamic pressure at a 0-deg angle of attack held constant at 8 $\mathrm{lb/ft^2}$ for all thrust coefficients. The specific details of the two comparison conditions are presented in Table 1.

The results for these cases are presented in Figs. 15–18. In both cases, the calculated results predict the lift and drag forces well for lower angles of attack, with reasonable accuracy even beyond the stall point, right through to 90 deg. Reference [27] also presents results for lower thrust coefficients of 0.50 and 0.20. As the thrust coefficient is reduced these cases show increasing errors (though the correct trends) for large poststall angles of attack, approaching 90 deg. This occurs for two reasons: First, the freestream velocity is significantly larger than the slipstream velocity increment and hence the angles of attack in the slipstream region are not small. (This is even true for the 0.71 thrust-coefficient case.) Second, due to the high nonslipstream dynamic pressure, the slipstream loads do not dominate those of the nonslipstream regions. In contrast, the higher-thrust-coefficient cases show better agreement when the slipstream loads do dominate and when the slipstream angles of attack are much lower. In practical terms, the two load cases at 90 deg can be thought of as representing different crosswind conditions on a hovering vehicle. Given that the actual T-wing test demonstrator has a disc loading of 9.53 $\mathrm{lb/ft^2}$ ($2v_{ia} = 89.5$ ft/s, standard sea-level conditions), the low-thrust-coefficient condition (0.71) corresponds to vertical hover in an unflyable crosswind of 104.6 ft/s (61.9 kt), and the high-thrust-coefficient condition (0.91) corresponds to a still-large but realistic crosswind of 38.5 ft/s (22.7 kt).¶ Thus, the poor performance at high angles of attack for low-thrust-coefficient cases is not a serious practical deficiency of the method.

The comparisons with [27] were found to be improved if the propeller slipstream velocities obtained from the blade-element calculations were replaced with constant axial-only distributions with a velocity increment of $2v_{ia}$, as given by Glauert's hypothesis [14,28]:

$$v_{ia}^4 + 2Vv_{ia}^3 \cos\alpha + v_{ia}^2 V^2 = \left(\frac{T}{2\rho A}\right)^2 \tag{8}$$

Although this observation may seem to invalidate some of the methodology presented, the inclusion of the swirl and axial velocity variations in the slipstream are important in particular cases. This is because with swirl added, the predominant loads are located on the side of the propeller slipstream velocity distribution in which the swirl adds to any onset velocities from crosswinds. This means that

---

¶In actual fact, during hover in a crosswind, the vehicle tilts into the wind, thus somewhat lessening the magnitude of the normal velocity component. To date, the concept-demonstrator vehicle has hovered in winds up to 30 ft/s.

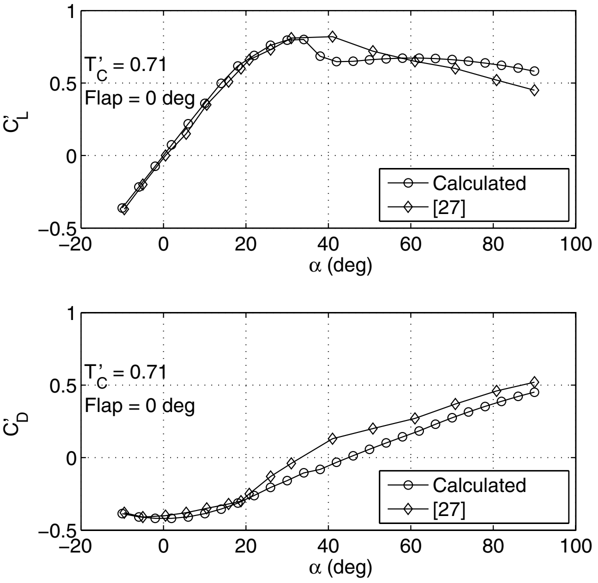

Fig. 15 Calculated and measured C_L' and C_D' for $T_C' = 0.71$ and $\delta_{\text{Flap}} = 0\,\text{deg}$.

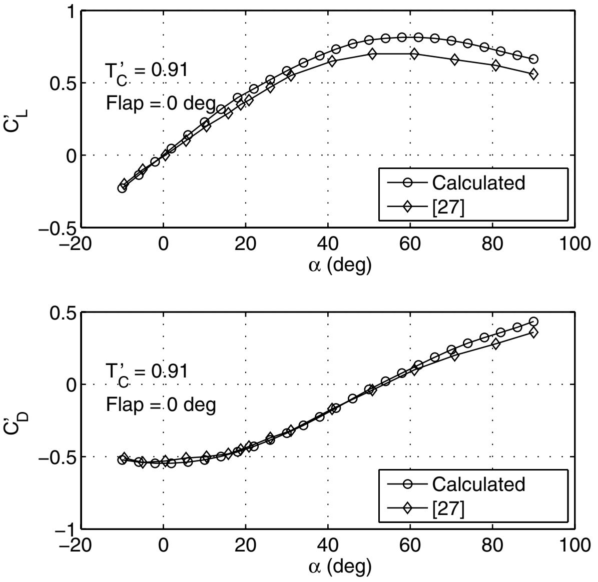

Fig. 16 Calculated and measured C_L' and C_D' for $T_C' = 0.91$ and $\delta_{\text{Flap}} = 0\,\text{deg}$.

if, for a particular vehicle, the wing ends within the propeller slipstream edge, then the vehicle will have a marked difference in flap effectiveness during hover, depending on the direction of the crosswind in which it is hovering. In MDO analysis of the vehicle, in which propeller position is free to vary spanwise as a design variable, this important consideration must be present to ensure that correct design sensitivities are generated.

V. Results for the T-Wing UAV Concept Demonstrator

The usefulness of the previously described methodology for the prediction of T-wing loads can be appreciated by looking at both individual load-case results and aggregate results from the simulation databases.

A. Individual Load-Case Results

Figure 19 shows the predicted lift and drag coefficients for a generic T-wing vehicle over a range of angles of attack from 0 to 90 deg. No power effects were included, and to simplify the discussion of the effects observed, the fins were deleted from the model. It should be noted that lift and drag coefficients were nondimensionalized with respect to wing-area alone, and hence the coefficients are slightly higher than might be expected, because the

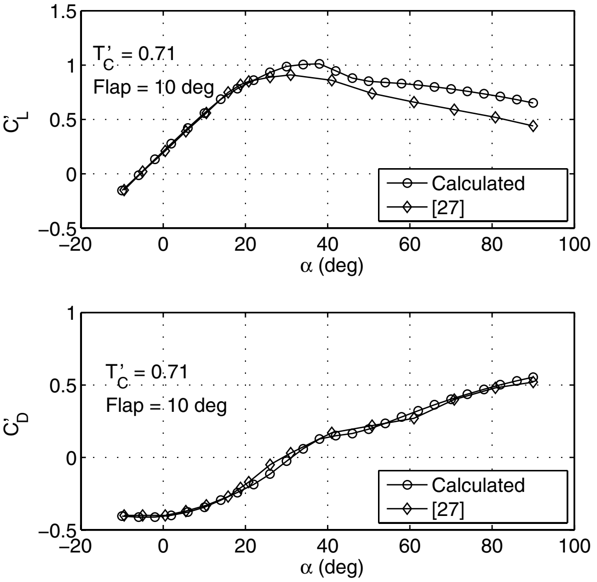

Fig. 17 Calculated and measured C_L' and C_D' for $T_C' = 0.71$ and $\delta_{\text{Flap}} = 10\,\text{deg}$.

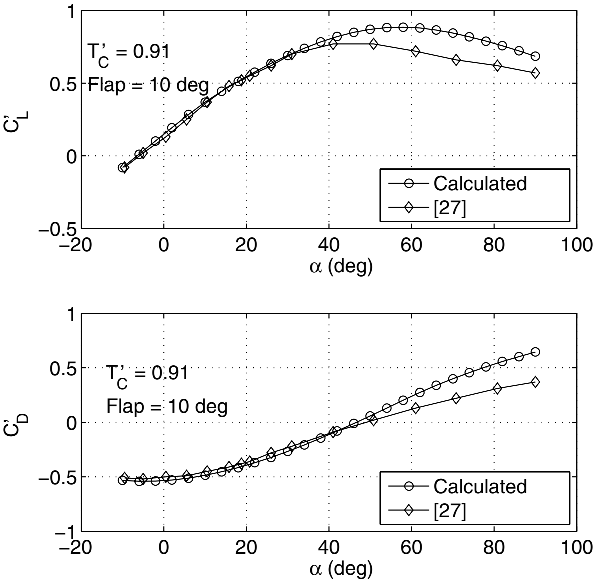

Fig. 18 Calculated and measured C_L' and C_D' for $T_C' = 0.91$ and $\delta_{\text{Flap}} = 10\,\text{deg}$.

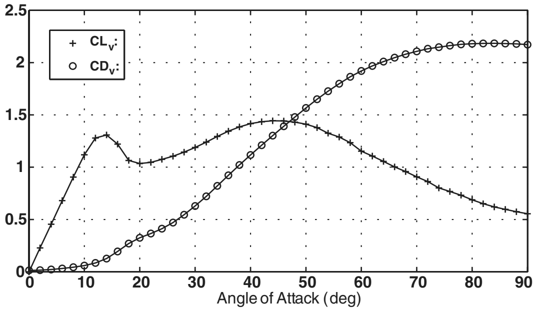

Fig. 19 Predicted lift and drag coefficients for a generic T-wing vehicle from a 0- to 90-deg angle of attack; no fins and no power effects.

canard is also producing both lift and drag. The following observations can be made about the data presented. The linear and parabolic nature of the lift and drag coefficients, respectively, at low prestall angles of attack is evident. Beyond the stall, which begins at about 10 deg, the lift coefficient initially drops and then rises again before eventually decreasing to ~0.55. Although the real lift coefficient of the aircraft should be zero at 90-deg angle of attack, this value is significantly better than the value of 7.4 for the uncorrected solution (not shown). In looking at the drag values, it can be seen that after the stall, the values increase to ~2.2 at the 90-deg condition. This is reasonable, because the drag of a wing section perpendicular to a flow is of about this magnitude [29].

Although it may seem that an error in lift coefficient of 0.55 for the 90-deg condition would be unacceptable, it should be noted that such angles of attack only apply to the nonslipstream regions during vertical flight. The loads in these regions are typically secondary compared with the slipstream-region loads, due to the large difference in dynamic pressure, and hence this level of error is tolerable.** Furthermore, the error in the nonslipstream lift loads is reflected as a perturbation to the X-direction loads when the vehicle is vertical, which are dominated by propeller thrust. The drag loads for the nonslipstream region, although probably not highly accurate, at least show the correct trend and provide the correct perturbations to the overall vehicle loading.

The next set of figures present predicted results for the actual concept-demonstrator vehicle, hovering vertically in a 20-ft/s crosswind, normal to its wings ($\alpha = 90$ deg). Pertinent physical information regarding this vehicle is given in Table 2. The aerodynamic grid is as shown in Fig. 11. It consists of 32 spanwise panel in the wing zones and six chordwise panels. Figure 20 presents the input velocity field over the starboard wing for this vehicle. The slipstream region is clear, with the external flows fixed at 20 ft/s. The reason that the inboard lobe of the propeller velocity distribution is slightly higher than the outboard lobe is that in this region the swirl velocity adds to the external flow, whereas in the outboard region it subtracts from it. This slightly increases the magnitude of the total flow velocity vector on the inboard side. Figure 21 presents the input angle-of-attack distribution for this load condition. The effects of swirl in the propeller slipstream are more obvious here and give an increased angle of attack on the upgoing (inboard) side, on which the tangential propeller velocities add to the onset crosswind velocity, with values ranging between 20 and 40 deg. Some stalling would thus be expected on this side of the slipstream. On the outboard side, the swirl velocities cancel the onset flow for the major part of the slipstream radius. Outside the propeller slipstream, the input angle of attack is 90 deg. Finally, Fig. 22 presents both the inviscid and viscous (corrected) panel-method loads per unit span along the starboard wing. As expected, some stalling is seen in the inboard lobe of the propeller distribution. The fact that the nonslipstream-region loads are only second-order perturbations during low-speed vertical flight compared with the slipstream-region loads is also clear from this figure. The importance of the viscous corrections is also evidenced by the gross errors in inviscid lift loads on the inboard nonslipstream part of the wing.

Although a similar level of accuracy may be obtained by treating the nonslipstream regions outside the panel-method code and simply using handbook values to obtain their lift and drag coefficients, this would offer a less unified solution strategy. The advantage of the approach used is that it allows for a seamless description of the vehicle aerodynamics using a consistent model and methodology from low-speed vertical flight right through to maximum horizontal flight speed conditions.

The fact that the method presented does offer this unified solution can be appreciated by considering Fig. 23, which shows the wing and canard inviscid and viscous (corrected) solutions for a 10-deg angle-of-attack condition. In this figure, the pairs of inviscid and viscous solutions for each surface are easily identified, with the inviscid solution always greater than the viscous solution. This particular graph is for a vehicle with a larger span canard than that of the concept demonstrator and with fins removed. In this case, the match between the corrected and raw solutions is seen to be good, except for stall effects starting to alter the center region of the canard solution. This is the region of highest effective angle of attack, due to the addition of the wing upwash on the local canard flow. Taken together with the previous discussion, this demonstrates that the 2-D

Table 2 Specifications for the T-wing concept demonstrator

Property	Value (Imperial)	Value (SI)
Wing span	7.142 ft	2.177 m
Wing chord	1.103 ft	0.336 m
Canard span	2.458 ft	0.749 m
Canard chord	0.472 ft	0.144 m
Propeller y position	1.993 ft	0.607 m
Propeller diameter	2.083 ft	0.635 m
Height (standing on ground)	5.000 ft	1.524 m
Engine power (per engine)	7.64 hp	5.70 kW
Takeoff weight	65.00 lb	29.48 kg

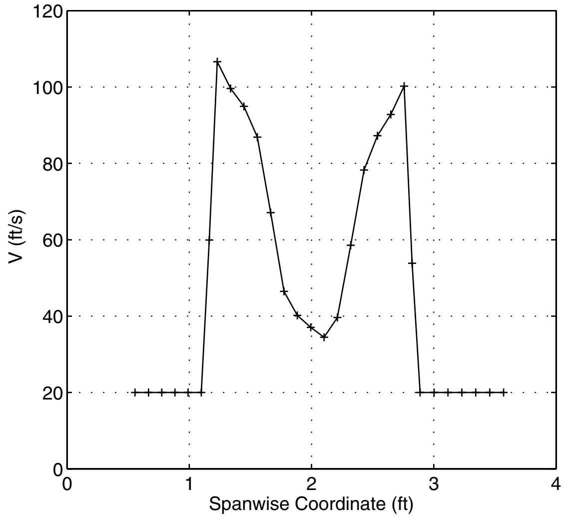

Fig. 20 Input velocity field over the starboard wing for the T-wing-type vehicle hovering in 20-ft/s wind.

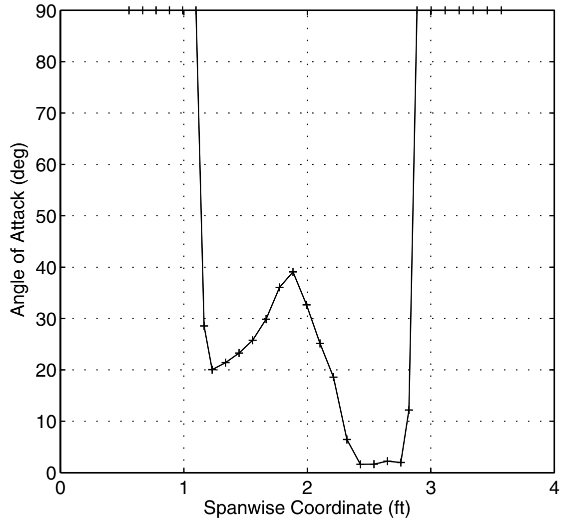

Fig. 21 Input angle of attack over the starboard wing for the T-wing concept-demonstrator vehicle hovering in 20-ft/s wind.

**For instance, for a 65-lb vehicle hovering with two 25-in.-diam propellers, the dynamic pressure in the far wake is 9.4 psf; for a 20-ft/s crosswind, the dynamic pressure is 0.48 psf. Allowing for the fact that the nonslipstream regions are approximately double the area of the slipstream regions, this still leaves an order-of-magnitude difference between loads produced in the two regions (assuming similar lift coefficients).

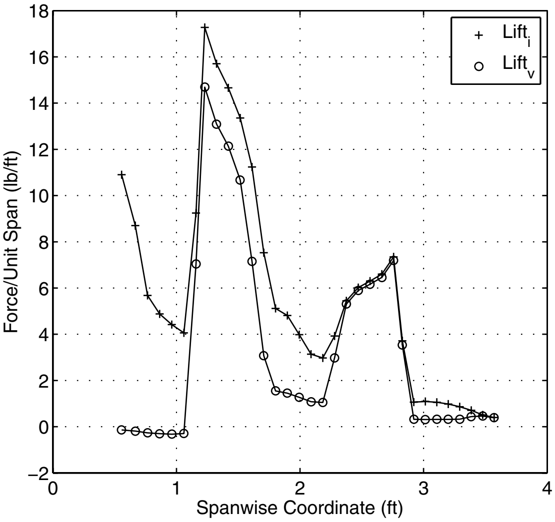

Fig. 22 Inviscid and viscous (corrected) lift distributions over starboard wing for the T-wing concept-demonstrator vehicle hovering in 20-ft/s wind; moderate-wing semispan grid of 32 × 6.

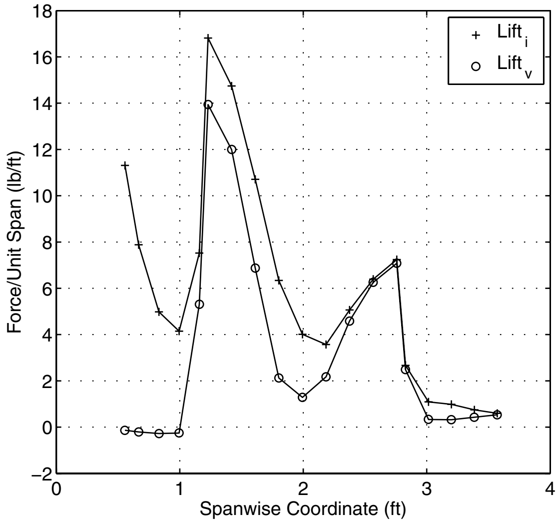

Fig. 24 Inviscid and Viscous (corrected) lift distributions over the starboard wing for the T-wing concept-demonstrator vehicle hovering in 20-ft/s wind; coarse-wing semispan grid of 18 × 3.

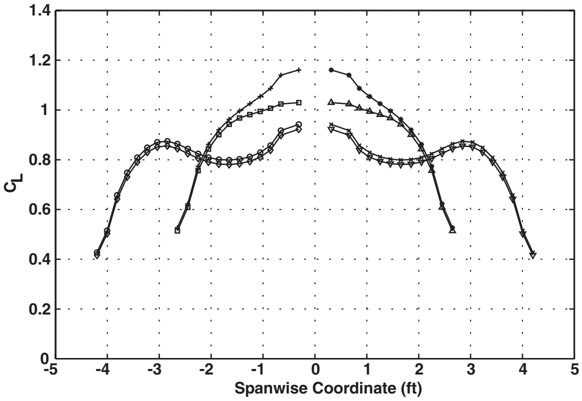

Fig. 23 Inviscid and viscous lift coefficients for wing and canard at $\alpha = 10$ deg (canard curves are shorter span).

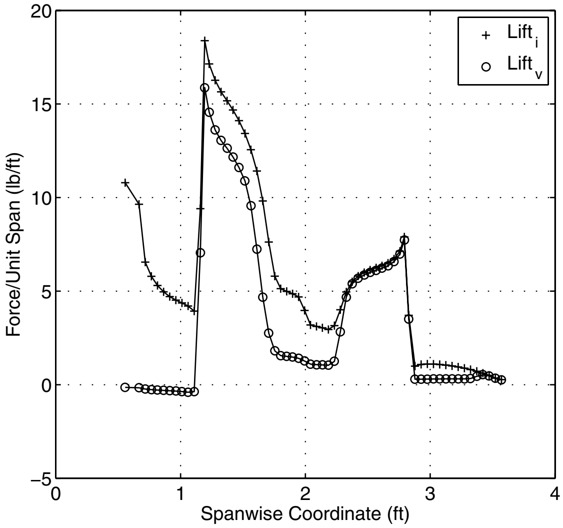

Fig. 25 Inviscid and viscous (corrected) lift distributions over the starboard wing for the T-wing concept-demonstrator vehicle hovering in 20-ft/s wind; fine-wing semispan grid of 62 × 12.

corrections easily blend between the inviscid solutions at lower angles while still giving some predictive capacity at flow angles well outside the range of applicability of regular panel-method solutions. (The standard effects of the canard inboard downwash and outboard upwash on the wing lift distribution are also seen in Fig. 23.) It should be noted that the accuracy of the inviscid flow solutions has been confirmed via comparison with handbook values found in Belotserkovskii [30].

B. Grid Refinement

As a check on the convergence of the results presented previously, solutions were also run at two other grid resolutions: approximately twice and half the panel size of those presented in Fig. 22. Only the final lift distributions are presented in Figs. 24 and 25. Integrated force and moment results for these three grid resolutions are given in Table 3. Only body-axis Z forces were given as the X-direction forces are dominated by propeller thrust. (Because of this, the X force results show *better* agreement than the Z force results: to within 1%.) As can be seen, in both qualitative and quantitative terms, there is little difference between the solutions (maximum divergence ~5% between any two). This suggests that for the dominant forces found in hover flight, even the coarse-grid solution would be acceptable.

C. Six-Degree-of-Freedom Simulation-Database Results

One of the most important uses for the aerodynamic model developed for the T-wing UAV has been the construction of a comprehensive aerodynamic database for use in simulation and flight control studies. Because of the difficulty of performing wind-tunnel tests on the configuration for powered vertical flight conditions, this is currently the sole source of aerodynamic data for the vehicle. The properties of these databases are given in Table 4.

Data extracted from a recent simulation database for the concept-demonstrator vehicle are presented in Figs. 26–28. The data are plotted as a set of four surfaces, corresponding to different throttle settings between 40 and 100% in 20% increments. In all cases, the parameters are shown varying with angle of attack and velocity, with zero sideslip. Figure 26 shows the variation in the body-axis X-direction force. As expected, this thrust force increases with the

Table 3 Grid convergence results. Grid densities ($m \times n$) refer to spanwise and chordwise panelization in the wing semispan

Solution type	Quantity	Coarse grid (18 × 3)	Medium grid (32 × 6)	Fine grid (62 × 12)
Inviscid	F_Z, lb	−30.47	−30.07	−30.53
Viscous	F_Z, lb	−24.43	−24.14	−24.21
Inviscid	M, ft · lb	−15.96	−15.14	−15.96
Viscous	M, ft · lb	−13.13	−12.50	−12.95

Table 4 Simulation databases

Database	Velocity range, ft/s	α and β range, deg	Throttle range
Low speed	−10 to 70	−90 to 90	0.35 to 1.00
High speed	70 to 190	−10 to 30	0.15 to 1.00

absolute value of flow angle. Figure 27 shows the body-axis Z force, with stall behavior clear at higher angles of attack. Figure 28 shows the pitching moment due to elevon derivative; the main feature of this graph is the increased effectiveness with increased throttle.

For the lower velocities, the data are believed to well describe the aerodynamic properties of the T-wing vehicle. At the more extreme combinations of velocity and angle of attack, however, the data become increasingly suspect as some of the previously mentioned assumptions begin to be violated. For instance, at 40 ft/s and 90-deg angle of attack, the loads in the nonslipstream regions are no longer minor compared with the slipstream loads. What is more, significant stalling within the slipstream is also expected in this condition. The limitations due to these factors are particularly evident in the extreme corners of the elevon pitching-moment derivative plot (Fig. 28).

VI. Conclusions

This paper has described the methodology used to predict the aerodynamic loads for a relatively unique wing-in-slipstream UAV. This was done via a combined blade-element and fixed-wake panel-method model. The method presented covers the full operating envelope of the UAV in a consistent and efficient manner that has allowed it to be used for MDO work and the construction of large simulation aerodynamic databases. One particular feature of the analysis is the correction of the inviscid panel-method solution with 2-D experimental data. Although there are clear limitations with this approach, it was shown to be useful within the context of the current UAV model in eliminating gross errors for those regions well outside the bounds of standard potential flow solutions.

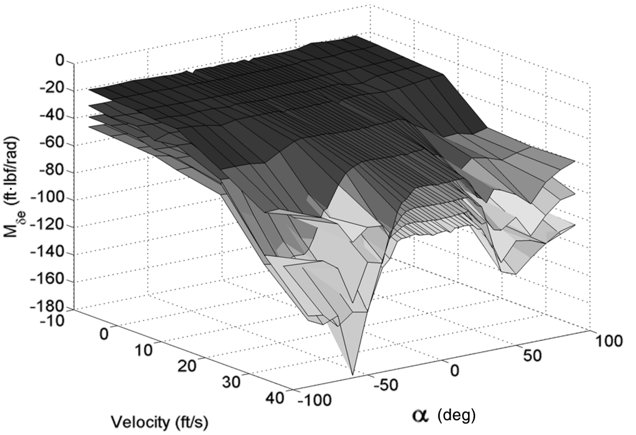

Fig. 28 Pitching moment due to elevon vs angle of attack and velocity at four throttle settings: 0.4, 0.6, 0.8, and 1.0.

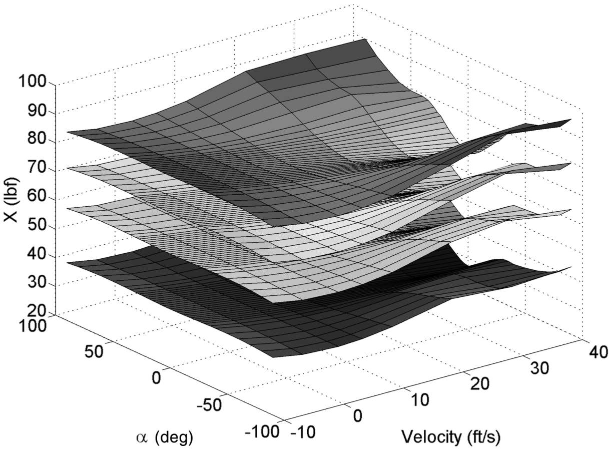

Fig. 26 Body-axis X force vs angle of attack and velocity at four throttle settings: 0.4, 0.6, 0.8, and 1.0.

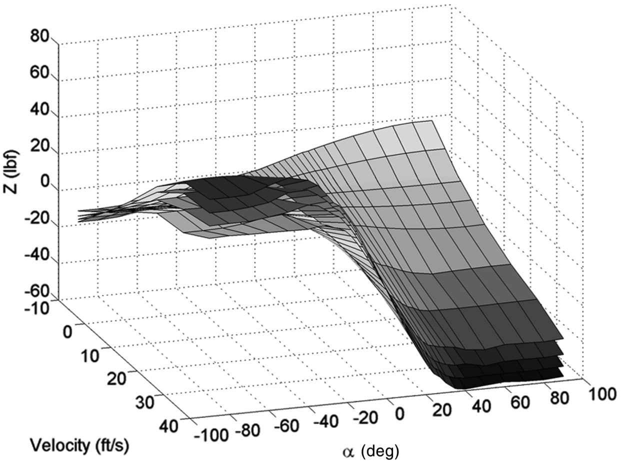

Fig. 27 Body-axis Z force vs angle of attack and velocity at four throttle settings: 0.4, 0.6, 0.8, and 1.0.

Acknowledgments

This work was supported by the Commonwealth Government of Australia and Sonacom Pty, Ltd., through the Strategic Partnership with Industry — Research and Training (SPIRT) grant C89906759, awarded in 1999. Sonacom Pty, Ltd., has also provided ongoing support to this program. During 2004 and 2005, some control-related aspects of this project were funded via the U.S. Air Force Office of Scientific Research, contract number AOARD-044031.

References

[1] Stone, R. H., “Configuration Design of a Canard Configured Tail-Sitter Unmanned Air Vehicle Using Multidisciplinary Optimisation,” Ph.D. Dissertation, Department of Aeronautical Engineering, Univ. of Sydney, Sydney, Australia, 1999.

[2] Munson, K., *Jane’s Unmanned Aerial Vehicles and Targets*, Jane’s Information Group, Surrey, England, U.K., 1998.

[3] Albion, N., The Boeing Company, Seattle, WA, “Vertically Launchable and Recoverable Winged Aircraft,” U.S. Patent No. 5,765,783, issued 16 June 1998.

[4] Bridgman, L., *Jane’s All The World’s Aircraft 1954-55*, Jane’s All The World’s Aircraft Publishing Company, London, 1955, p. 227.

[5] Bridgman, L., *Jane’s All The World’s Aircraft 1955-56*, Jane’s All The World’s Aircraft Publishing Company, London, 1956.

[6] McVeigh, M. A., Gray, L., and Kisielowski, E., “Prediction of Span Loading of Straight-Wing/Propeller Combinations up to Stall,” NASA CR-2602, 1975.

[7] Kroo, I., “Propeller–Wing Integration for Minimum Induced Loss,” *Journal of Aircraft*, Vol. 23, No. 7, 1986, pp. 561–565.

[8] Witkowksi, D. P., Lee, A. K. H., and Sullivan, J. P., “Aerodynamic Interaction Between Propellers and Wings,” *Journal of Aircraft*, Vol. 26, No. 9, 1989, pp. 829–836.

[9] Ardito Marretta, R. M., “Performance of a Propeller Embedded in the Flowfield of a Wing,” *Journal of Aircraft*, Vol. 33, No. 5, 1996, pp. 919–923.

[10] Ardito Marretta, R. M., “Different Wing Flowfields Interaction on the Wing-Propeller Coupling,” *Journal of Aircraft*, Vol. 34, No. 6, 1997, pp. 740–747.

[11] Ardito Marretta, R. M., Davi, G., Milazzo, A., and Lombardi, G., “Wing Pitching and Loading with Propeller Interference,” *Journal of Aircraft*, Vol. 36, No. 2, 1999, pp. 468–471.

[12] Favier, D., Ettaouil, A., and Maresca, C., “Numerical and Experimental Investigation of Isolated Propeller Wakes in Axial Flight,” *Journal of Aircraft*, Vol. 26, No. 9, 1989, pp. 837–846.

[13] Simonetti, F., and Ardito Marretta, R. M., "A Numerical Variational Approach for Rotor-Propeller Aerodynamics in Axial Flight," *Computer Modeling and Simulation in Engineering*, Vol. 1, No. 3, 2000, pp. 81–90.

[14] McCormick, B. W., *Aerodynamics of V/STOL Flight*, 1st ed., Academic Press, New York, 1969.

[15] Ardito Marretta, R. M., Davi, G., Milazzo, A., and Lombardi, G., "Wing Propeller Coupling Simulation from Tractor to Hover Flight Conditions," *Computer Modeling and Simulation in Engineering*, Vol. 2, No. 3, 1997, pp. 304–321.

[16] Hunsaker, D., and Snyder, D., "A Lifting-Line Approach to Estimating Propeller/Wing Interactions," 24th Applied Aerodynamics Conference, San Francisco, CA, AIAA Paper 2006-3466 , 2006.

[17] Phillips, W. F., and Snyder, D. O., "Modern Adaptation of Prandtl's Classic Lifting Line Theory," *Journal of Aircraft*, Vol. 37, No. 4, 2000, pp. 662–670.

[18] Stone, R. H., "Aerodynamic Modeling of a Wing-in-Slipstream Tail-Sitter UAV," International Powered Lift Conference, AIAA Paper 2002-5951, 2002.

[19] Stone, R. H., and Wong, K. C., "Preliminary Design of a Tandem-Wing Tail-Sitter UAV Using Multi-Disciplinary Optimization," *International Aerospace Congress 97*, The Royal Aeronautical Society, Australian Div., Sydney, Australia, 1997, pp. 707–720.

[20] McCormick, B. W., *Aerodynamics, Aeronautics and Flight Mechanics*, 2nd ed., Wiley, New York, 1995.

[21] Katz, J., and Plotkin, A., *Low-Speed Aerodynamics*, 2nd ed., Cambridge Univ. Press, Cambridge, England, U.K., 2001.

[22] Gallman, J. W., and Kroo, I., "Optimization of Joined Wing Aircraft," *Journal of Aircraft*, Vol. 30, No. 6, 1993, pp. 897–905.

[23] Gallman, J. W., Kaul, R. W., Chandrasekharan, R. M., and Hinson, M. L., "Optimization of an Advanced Business Jet," *Journal of Aircraft*, Vol. 34, No. 3, 1997, pp. 288–295.

[24] Critzos, C. K., Heyson, H. H., and Boswinkle, R. W., "Aerodynamic Characteristics of NACA 0012 Airfoil Section at Angles of Attack from 0° to 180°," NACA TN-3361, 1955.

[25] Hoak, D. E., *USAF Stability and Control Datacom*, Flight Control Div., U.S. Air Force Flight Dynamics Lab., Wright–Patterson AFB, OH, 1978.

[26] Torenbeek, E., *Synthesis of Subsonic Airplane Design*, Delft University Press, Delft, The Netherlands, and Kluwer Academic, London, 1988.

[27] Kuhn, R. E., and Draper, J. W., "An Investigation of a Wing–Propeller Configuration Employing Large-Chord Plain Flaps and Large-Diameter Propellers for Low-Speed Flight and Vertical Take-Off," NACA TN-3307, 1954.

[28] Glauert, H., "Airplane Propellers," *Aerodynamic Theory*, edited by Durand W F, Vol. 4, Dover, New York, 1963, pp. 318–320.

[29] Hoerner, S. F., *Fluid Dynamic Drag*, Hoerner Fluid Dynamics, Albuquerque, NM, 1965.

[30] Belotserkovskii, S. M., *Theory of Thin Wings in Subsonic Flow*, Plenum, New York, 1967.